# Indolocarbazole as a Platform for Concatenated Crystalline Rotors

Ernesto Hernández-Morales,[a] Abraham Colin-Molina,[a] Jessica Arcudia,[b] Federico J. Hernández,[c] Mario Rodríguez,[d] Ruben A. Toscano,[a] Rachel Crespo-Otero,[c*] Gabriel Merino,[b*] and Braulio Rodríguez-Molina[a*]

[a]Instituto de Química, Universidad Nacional Autónoma de México, Circuito Exterior, Ciudad Universitaria, Ciudad de México 04510, México

[b]Departamento de Física Aplicada, Centro de Investigación y de Estudios Avanzados, Unidad Mérida. Km. 6 Antigua Carretera a Progreso, Apdo. Postal 73, Cordemex, 97310, Mérida, Yuc., México.

[c] Department of Chemistry, University of College London, 20 Gordon Street, London WC1H 0AJ, UK

[d]Research Group of Optical Properties of Materials (GPOM), Centro de Investigaciones en Óptica, CIO, Apdo., Postal 1-948, 37000 León Gto, México.

r.crespo-otero@ucl.ac.uk

gmerino@cinvestav.mx

brodriguez@iquimica.unam.mx

## Abstract

Herein we describe a series of molecular rotors formed by the cocrystallization of three indolo[3,2-*b*]carbazole (ICZ) derivatives with butyl and cyclohexyl substituents, along with 1,4-diaza[2.2.2]bicyclooctane (DABCO). The structures of rotors **I** and **III** were confirmed through single-crystal X-ray diffraction (SCXRD), revealing a concatenated 1D arrangement between the two components. Variable temperature VT SCXRD experiments on rotors **I** and **III** suggested that the rotator shows rotational motion, with activation energies of 6.8 and 1.8 kcal $mol^{-1}$, respectively. The lower *Ea* for rotor **III** was attributed to the flexible environment around DABCO due to the cyclohexyl groups, while the surroundings of rotor **I** were found to be more rigid. Additionally, our predictions of radiative and nonradiative (IC and ISC) decay constants indicate that the vibrations of the molecular rotors impact nonradiative decay rates and, consequently, the fluorescence quantum yields.

## Introduction

Molecular motion is closely associated with various fascinating properties in the solid state, including dielectric response in charge transfer cocrystals,[1] birefringence,[2] salient effects,[3] thermal expansion,[4] and single crystal to single crystal transitions.[5] Controlling the mobility in crystalline materials holds the potential to modulate these properties. Our research group focuses on the study of intramolecular rotation in crystalline materials, with a particular interest in constructing molecular rotors through crystal/cocrystal engineering.[6]

The cocrystallization strategy is a promising approach to develop new fluorescent compounds because it leverages the complementarity of the components to minimize noncovalent interactions and facilitate rapid motion.[15] Such fast internal mobility is expected to regulate the emissive properties of the materials. Particularly, the motion-emission relationship is commonly used to explain why π-conjugated molecules which are non-emissive in dilute solutions, become highly fluorescent in

aggregates or in the solid state.[7] This phenomenon is termed Aggregation-Induced Emission (AIE) and it relies in the restriction of intramolecular motion (RIM) model.[8] Therefore, if the conditions are appropriate, the intramolecular motion may generate molecular rotation-induced emission quenching.[9] Examples of highly mobile components that cause fast non-radiative relaxation[10] are carboranes,[11] fast rotating phenylenes,[12] pyridines,[13] or tetraphenylethenes,[14] among others.

In a previous work, we have studied the intramolecular motion in discrete cocrystals assembled by hydrogen bonds between carbazoles and 1,4-diaza[2.2.2]bicyclooctane (DABCO).[16–18] The cylindrical shape of DABCO makes it an excellent candidate for rotatory components due to its low energy and volume-conserving motion.[19] Moreover, the strong basicity of its nitrogen atoms enables effective hydrogen bond acceptor capabilities.[20,21] Building upon this foundation, we aimed to explore the pairing of DABCO with a more conjugated component than carbazole, creating one-directional crystalline molecular rotors. While a few examples of 1D rotors have been reported in the literature,[22,23] the study of the resulting emissive properties of these crystals remains unexplored, making it an intriguing area for further exploration.

Indolocarbazoles (ICZ) are a series of five fused heterocycles formed by the fusion of carbazole and indole. These compounds exhibit exciting optical properties and can be distinguished from each other based on the relative position of the carbazole and indole components.[24] In the field of crystal engineering, McGillivary,[25] Perepichka,[26] and Hu[27] have reported novel crystalline materials using a specific isomer, 5,12-dihydroindolo[3,2-*a*]carbazole. This isomer has two NH groups that point in the same direction, making it an excellent hydrogen-bond donor. Exploiting this feature, they successfully created discrete cocrystals with strong aromatic stacks, leading to complementary Donor-Acceptor (D-A) intermolecular interactions or enhanced charge transport.

In our case, we aim to integrate the intramolecular dynamics of ICZ with its emissive properties within a 1D lattice structure. To achieve this, we focused on indolo[3,2-

*b*]carbazole, the only isomer that shows two NH groups pointing in antiparallel directions. This unique arrangement allows for the formation of a concatenated array of rotors through N-H···N hydrogen bonds with DABCO, as depicted in Figure 1. Considering that the solubility of this ICZ isomer could influence the crystallization experiments, we also explored the inclusion of aliphatic substituents in its periphery. Our purpose was to enhance solubility while preserving the intact hydrogen donor groups in the planar component of the molecule.

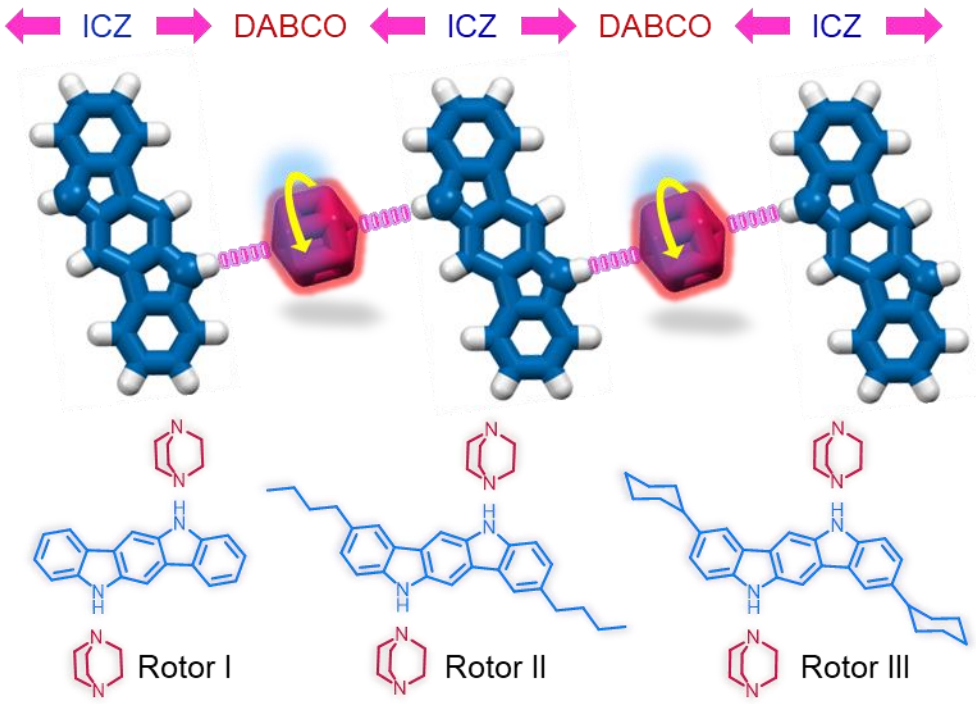


**Figure 1**. One-dimensional molecular rotors reported in this work obtained through cocrystallization between indolo[3,2-*b*]carbazoles and DABCO. The pink arrows highlight the proposed hydrogen bond interactions.

In this work, we present the cocrystallization of three indolocarbazole derivatives (**ICZ, But-ICZ,** and **Cy-ICZ**) with **DABCO**, resulting in the formation of three cocrystals: indolo[3,2-*b*]carbazole:DABCO (**I**), *bis*(butyl)-indolo[3,2-*b*]carbazole:DABCO (**II**), and *bis*(cyclohexyl)-indolo[3,2-*b*]carbazole:DABCO (**III**). The new solid samples were subjected to detailed characterization, as described below.

***Design, synthesis, and characterization of ICZ derivatives***

To prepare the rotors, we initiated the synthesis of indolo[3,2-*b*]carbazole (**ICZ**), *bis*(butyl)-indolo[3,2-*b*]carbazole (**But-ICZ**), and the new compound *bis*(cyclohexyl)-indolo[3,2-*b*]carbazole, following a classical double Fisher indolization method,[28] using the corresponding phenylhydrazine, outlined in Scheme S1 and Scheme S2. Since the molecular structure of the unsubstituted indolocarbazole (**ICZ**) has been previously reported,[29] our focus was on growing single crystals of the structure that are not available in the *Cambridge Crystallographic Data Centre* (CCDC): **But-ICZ** and new **Cy-ICZ**. Contrary to our initial expectation of improved solubility compared to **ICZ**, they exhibited low solubility in common organic solvents. However, we were able to prepare saturated solutions of both compounds in hot DMF or DMSO, facilitating the growth of suitable single crystals for X-ray diffraction experiments.

The molecular structure of **But-ICZ** was collected at 150 K, and the data were indexed and refined in a monoclinic $P2_1/c$ space group (Figure S1). Structural analysis showed a herringbone packing with an angle of 50.44° between the molecular planes. Each molecule of **But-ICZ** is surrounded by four neighboring molecules, forming CH···π and NH···π interactions, with a centroid-centroid distance of 6.48 Å and a centroid-plane distance of 2.51 Å. On the other hand, **Cy-ICZ** crystallized in two solvate forms (Figures S2 and S3) labeled as **Cy-ICZ:DMF** ($P2_1/n$, collected at 150 K) and **Cy-ICZ:DMSO** (*P*-1, collected at 298 K). In both crystal structures, the N-H groups are involved in N-H···O hydrogen bonds with the occluded solvent.

Initial cocrystallization experiments using the three indolocarbazole derivatives showed that their solubility in polar aprotic solvents (e.g., < 10 mg/mL in DMF) was significantly lower than that of DABCO (40 mg/mL in DMF). Therefore, a simple 1:1 mixture of the two components resulting in the precipitation (segregation) of the compound with the lower solubility, while DABCO remained in the solution. To achieve successful cocrystallization, we employed the supersaturation approach or reaction crystallization method[30] by using an excess of DABCO to saturate the initial solutions of the indolocarbazole derivatives. These experiments allowed the growth

of single crystals of rotors **I** and **III**, suitable for X-ray diffraction studies, as described in detail below.

**Concatenated rotors between indolocarbazoles and DABCO (rotors I and III)**

Crystals of rotor **I** suitable for X-ray diffraction analysis were obtained from a DMSO solution containing **ICZ** and DABCO with a 1:12 stoichiometry, as described in the *Supporting Information*. The data were collected at 298 K, and the structure was solved in a monoclinic $P2_1/n$ space group. Gratifyingly, we observed the desired interactions between **ICZ** and **DABCO** with a 1:1 stoichiometry. In rotor **I**, the two hydrogen bonds are crystallographically equivalent and oriented in opposite directions, with NH···N distances of 2.00(2) Å and an angle of 161(2)°, as depicted in Figure 2a. The molecules arrange themselves in an infinitely staggered manner, promoting the formation of layers (**Figure *2***c), with the neighboring ICZ components creating a square cavity around the heavily disordered DABCO framework (**Figure *2***d and Figure *S4)*. We also successfully grew single crystals of the concatenated molecular rotor **III**, which was refined in a monoclinic $P2_1/c$ space group at room temperature. The structural analysis revealed that DABCO is linked to the **Cy-ICZ** stators through strong N-H···N hydrogen bonds, with H···N 2.02(3) Å and a donor-H···acceptor angle of 167(2)º (**Figure *2***b). In rotor **III**, the two components lie virtually in the same plane, forming a one-directional array that propagates along the crystallographic *c*-axis (**Figure *2***d), where DABCO occupies a rhombohedral cavity created by the neighboring **Cy-ICZ** molecules (**Figure *2***f and Figure *S5*). In both cases, we observed crystallographic disorder in DABCO with an occupancy of 50 %. Despite our extensive efforts, we were unable to obtain single crystals of rotor **II** after multiple cocrystallization attempts. Therefore, we characterized the solid obtained through liquid-assisted grinding (LAG) using complementary spectroscopic techniques, as described in the subsequent sections.

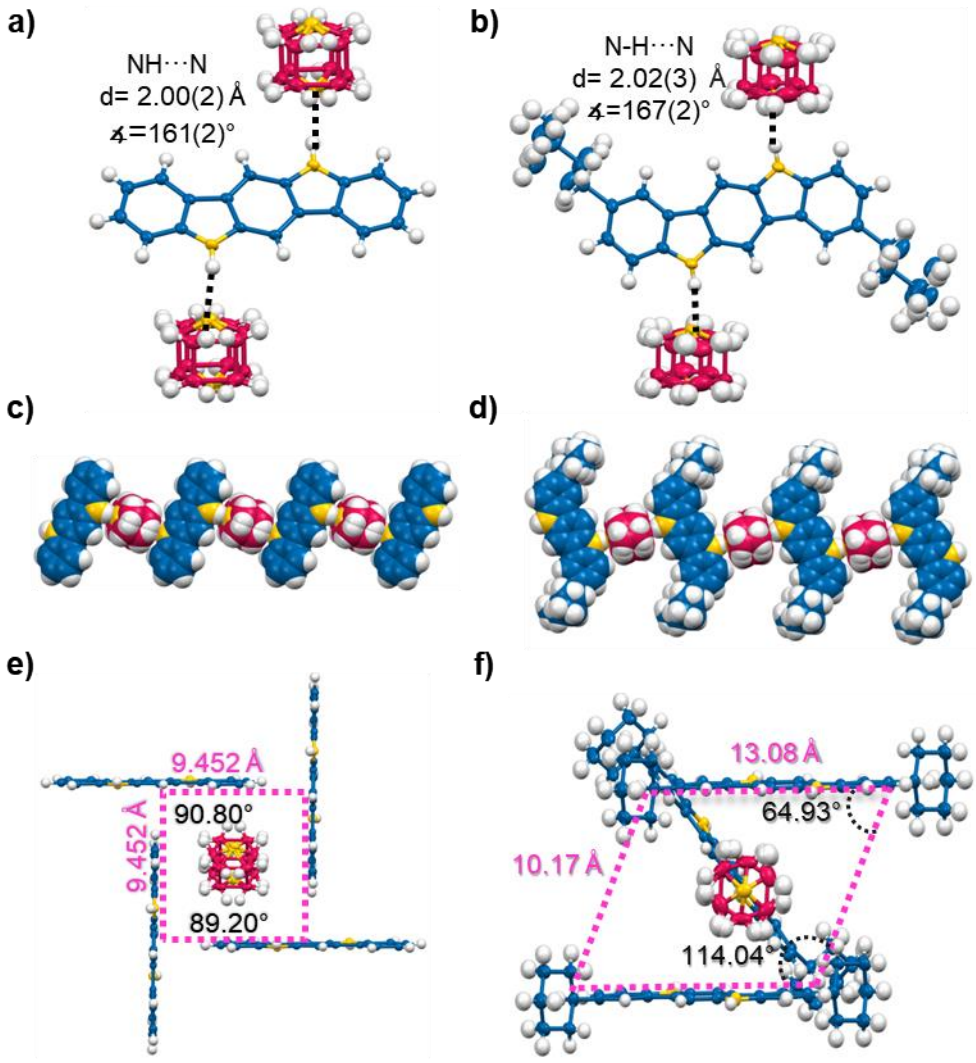


**Figure 2.** Single crystal structures of rotors **I** and **III** at 298 K. Hydrogen bond parameters of a) rotor **I** and b) rotor **III**. Representation of the desired 1D molecular chain of c) rotor **I** and rotor **III** d). Cavities surrounding DABCO in e) rotor **I** and f) rotor **III**.

After confirming the molecular structure of the rotors, we conducted variable temperature single-crystal X-ray diffraction experiments (VT-SCXRD) to investigate potential changes in the crystal structures (**Figure *3***). The diffraction data were collected at temperatures of 100, 150, 200, and 250 K for rotor **I**. As anticipated, decreasing the temperature resulted in smaller thermal ellipsoids for DABCO (**Figure *3***c). Notably, the structures at 150 K and 100 K were solved without observing disorder in this component. For rotor **III**, the attached cyclohexyl fragments

also exhibited ordering at low temperatures, indicating thermal mobility in this region at room temperature. (**Figure *3***a and 3b)

Unexpectedly, both rotors I and III showed a thermally driven single-crystal to single-crystal transformation (SCSC), known as a class transition. At room temperature, rotor **I** crystallized in centrosymmetric space group $P2_1/n$, while rotor **III** crystallized in centrosymmetric space group $P2_1/c$. However, at 150 K, the space group changed to a non-centrosymmetric $P2_1$ for both rotors. At 298 K, DABCO and **ICZ** crystallized with an inversion center, while at lower temperatures, the symmetry broke, likely due to the changes in the mobility of DABCO. It is noteworthy that this phase transition is highly unusual in molecular solids and is characterized by the preservation of crystal integrity. In other cases, such transitions have been associated with changes in various physical properties, such as ferroelectricity.[31–33]

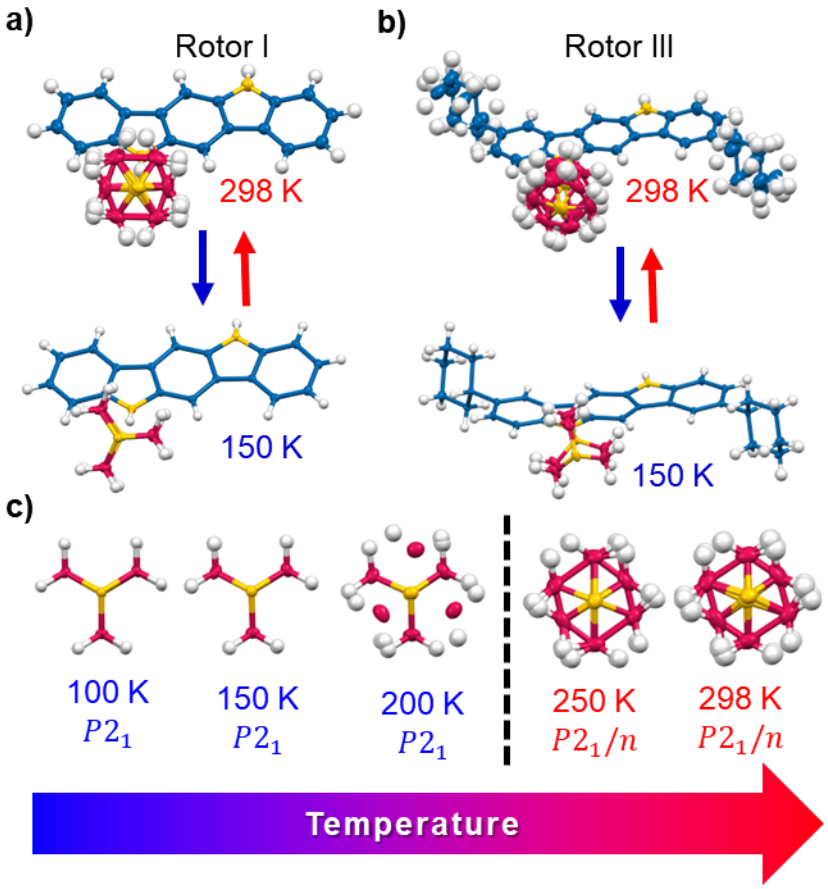


**Figure 3.** Variable temperature single crystal X-ray diffraction of the molecular rotors. Comparison at 298 K and 150 K of a) rotor **I** and b) rotor **III**, c) Changes in

the thermal ellipsoids of DABCO in rotor **I**. The dashed line indicates the observed class transition.

The temperature-dependent changes in crystallographic symmetry were accompanied by significant alterations in hydrogen bond parameters, as summarized in *Table S1* and *S2*. At low temperatures (150 K), both rotors exhibited similar hydrogen bond parameters, but the hydrogen bonds in antiparallel directions displayed differences (Figures *S6* and *S7)*. The structural transformation occurring during the cooling process provokes a straightening of the N-H···N bonds, resulting in a slight contraction of the unit cell volume. For rotor I, the unit cell volume decreased from 941.012 $Å^3$ at 298 K to 918.806 $Å^3$ at 150 K, while for rotor III, it decreased from 1533 $Å^3$ at 298 K to 1493 $Å^3$ at 150 K. Molecular overlays of the cocrystals of rotors I and III at 298 K and 150K (Figures S6-S8) indicate minor changes in crystal packing, which can be attributed to the shortened distance between DABCO and the corresponding indolocarbazoles.

### *Solid-state NMR $^{13}$CP-MAS and powder X-ray diffraction*

Once the molecular structure of rotors **I** and **III** was confirmed through X-ray diffraction experiments, we proceeded to gently crush a significant amount of single crystals (*ca.* 100 mg) for further analysis using powder X-ray diffraction (Figures S10-S12) and solid-state NMR $^{13}$C CPMAS (ssNMR). These techniques were employed to determine spectroscopic variations between the stators (**ICZs**) and the newly formed rotors. In particular, these techniques allowed us to complement the characterization of rotor **II,** for which we were unable to obtain single crystals suitable for X-ray diffraction.

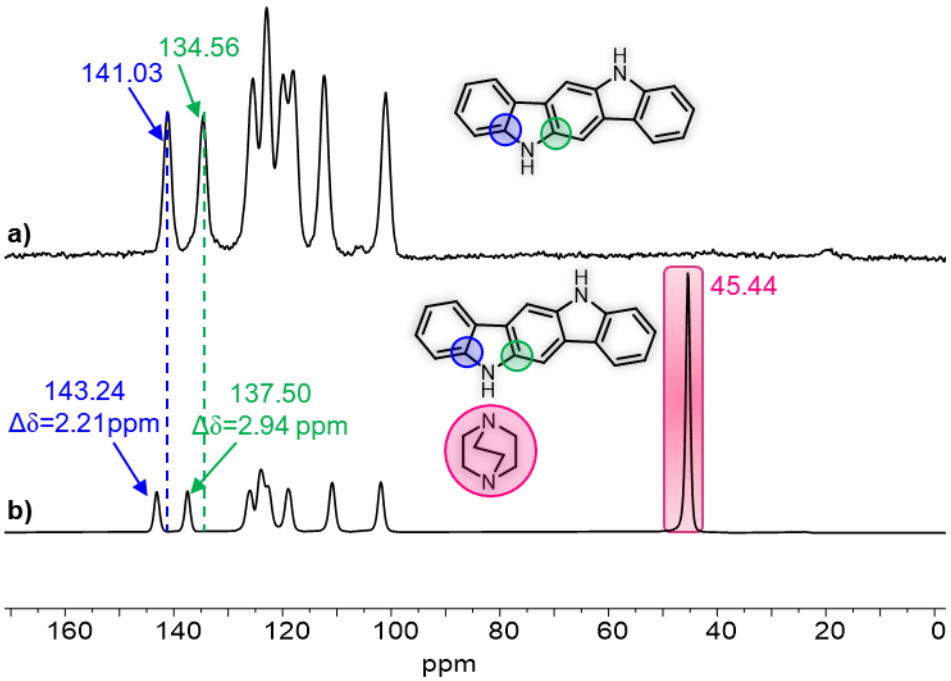


**Figure 4.** Solid-state $^{13}$C NMR CPMAS of a) **ICZ** and b) rotor **I**. The annotated chemical shifts and the dashed lines indicate the changes in the chemical shifts of the carbon atoms of **ICZ**, highlighted in blue and green. The signal corresponding to the carbon atoms in **DABCO** is highlighted in magenta.

The comparison of the $^{13}$C NMR spectra enabled the identification of changes between the **ICZ** stator and rotor **I**. The number of peaks observed corresponds to the asymmetric unit Z'=1 as shown in Figure S9. The spectra show noticeable changes in the chemical shifts, particularly in the signals associated with the carbons adjacent to the nitrogen atoms ($\Delta\delta$ = 2.21 and 2.94 ppm). These changes are attributed to the formation of a new hydrogen bond between **ICZ** and **DABCO**. Similar changes were observed in the solid obtained after cocrystallization of the **BUT-ICZ** derivative with **DABCO** (Figure S13), showing changes of 2.3 and 4.0 ppm for the carbon signals. Larger chemical shift changes were observed for rotor **III**, which displayed a greater number of peaks corresponding to the asymmetric unit exhibited in the single crystal structure (*Z*' = 0.5), as shown in Figure S14.

***Dynamic characterization by periodic DFT calculations and deuterium solid-state NMR***

Based on the cavity surrounding DABCO in rotors **I** and **III**, as well as the crystallographic disorder, it appeared plausible that these rotors undergo rapid internal dynamics. To evaluate this hypothesis, we employed density functional theory (DFT) computations and the nudged elastic band method[34] to gain initial insights into the rotational behavior of rotors **I** and **III** using X-ray data at room temperature. This computational approach has proven reliable in describing the intramolecular rotation of other cocrystals.[16–18] The calculated rotational potentials show that both rotors experience fast jumps of DABCO with local minima occurring every 60º (**Figure *5***). However, there is a significant difference in the calculated activation energies for rotation ($E_a$) between the two rotors. Rotor **I** shows a barrier of $E_a$= 6.8 kcal mol$^{-1}$, whereas rotor **III** has a much lower barrier of $E_a$= 1.8 kcal mol$^{-1}$.

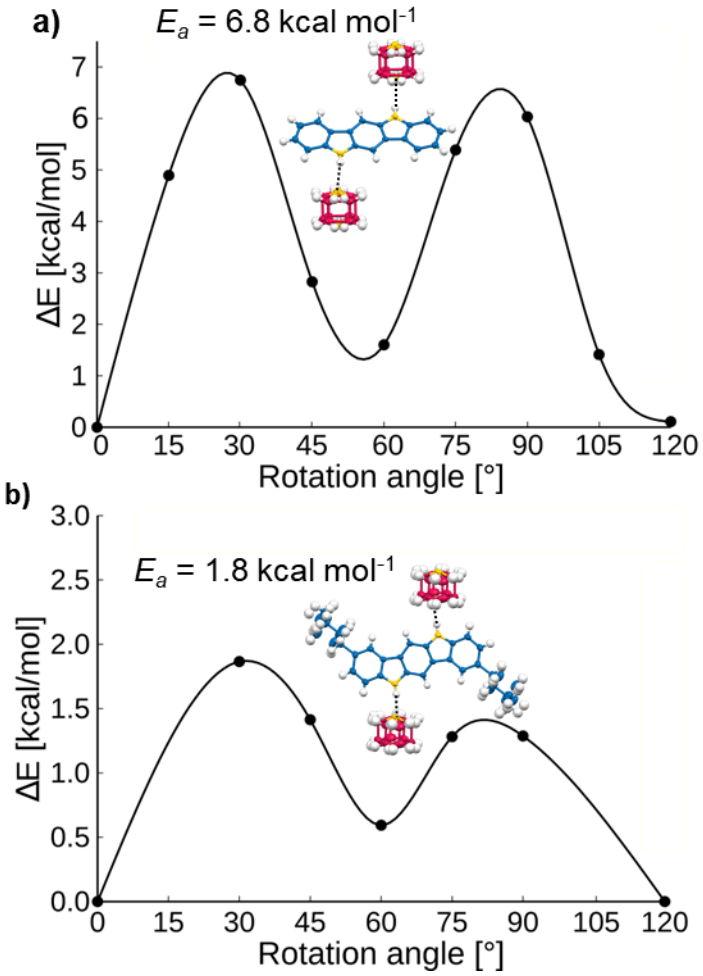


**Figure 5.** Rotation potential for rotors a) **I** and b) **III**. Both cases exhibited fast jumps with local minima at 60º, with a significant difference in the barrier to rotation of 6.8 kcal mol$^{-1}$ and 1.8 kcal mol$^{-1}$, for rotors **I** and **III**, respectively.

To elucidate the disparity in the activation barrier to rotation, we analyzed the noncovalent interactions (NCI) within the crystals using the NCIPLOT program.[35,36] The height of the rotational potential of rotor **I** could be attributed to the crystallographic symmetry around the DABCO component, as shown in **Figure *6***. The analysis reveals three types of contacts between neighboring **ICZ** and the methylene groups of DABCO: (1) interactions with the aromatic cloud of the terminal rings (Figure 6a), (2) interactions involving the C-H of the **ICZ** (Figure S16), and (3) interactions through the hydrogen bond (N/H) between the rotator and stator (Figure

S17). Hence, the rigid environment surrounding the rotatory portion may contribute to a high barrier to rotation.

In contrast, the rotational potential of rotor **III** is less symmetric (**Figure *5***b), with two distinct energy maxima. The NCI analysis shows three types of contacts: (1) the hydrogen bond (N/H) between the rotator and stator (Figure S18), (2) contacts between the methylene groups of DABCO and the aromatic rings of the **Cy-ICZ** stator (**Figure *6***b) and (3) multiple C-H interactions involving adjacent cyclohexyl groups (Figure S19). By considering the DFT and X-ray data collectively, it appears plausible that the lower $E_a$ in rotor **III** arises from the conformational flexibility of the cyclohexyl fragment encompassing the rotatory component, in contrast to the rigid environment found in rotor **I**.

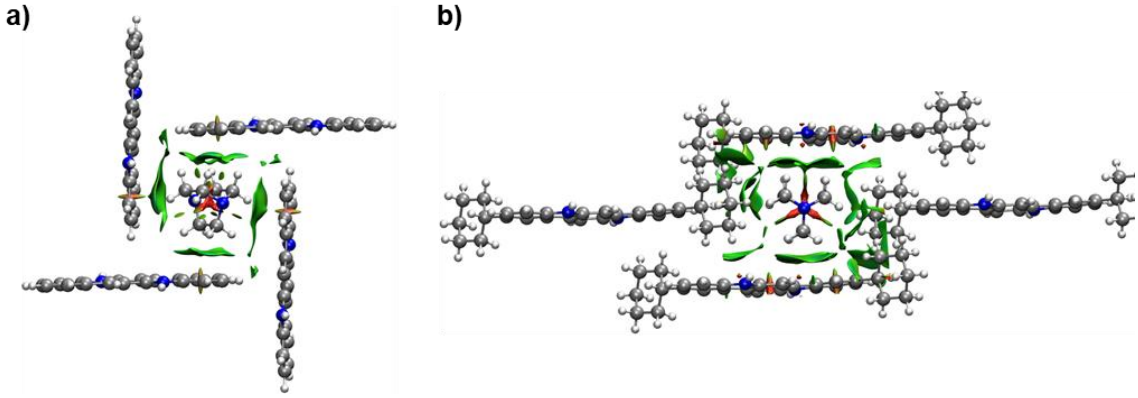


**Figure 6.** Intermolecular interactions founded in a) rotor **I** and b) rotor **III**. The environment in rotor **I** is rigid, while the cyclohexyl groups in rotor **III** create a flexible environment that might facilitate the motion of DABCO.

Based on the X-ray and computational findings, we carried out a dynamic characterization using $^{2}$H solid-state NMR.[37] Our focus was on rotor **I**, which exhibits the highest rotation barrier, for two reasons. Firstly, the timescale of this technique (1E$^{3}$ to 1E$^{6}$ Hz)[38] may not be sufficient to detect the motion of DABCO at higher frequencies, as expected in the case of rotor **III**. Secondly, the available spectrometer has a lower temperature limit of 248 K, which imposed limitations on the analysis. Despite these technical challenges, we considered that gathering the experimental solid-state NMR data for **I** would strongly support our DFT computations.

An isotopically enriched rotor **I** was prepared by using partially deuterated DABCO (see *Supporting Information*). We obtained a good amount of the deuterated rotor (50 mg) by following the same procedure used for the natural abundance one. Subsequently, we confirmed the phase purity of the enriched rotor through powder X-ray diffraction (Figure S10). The corresponding $^{13}C$ CPMAS spectra of the deuterated rotor closely matched those of the natural abundance counterpart (Figure S15). Note that the signal intensity of DABCO decreases due to partial deuteration.

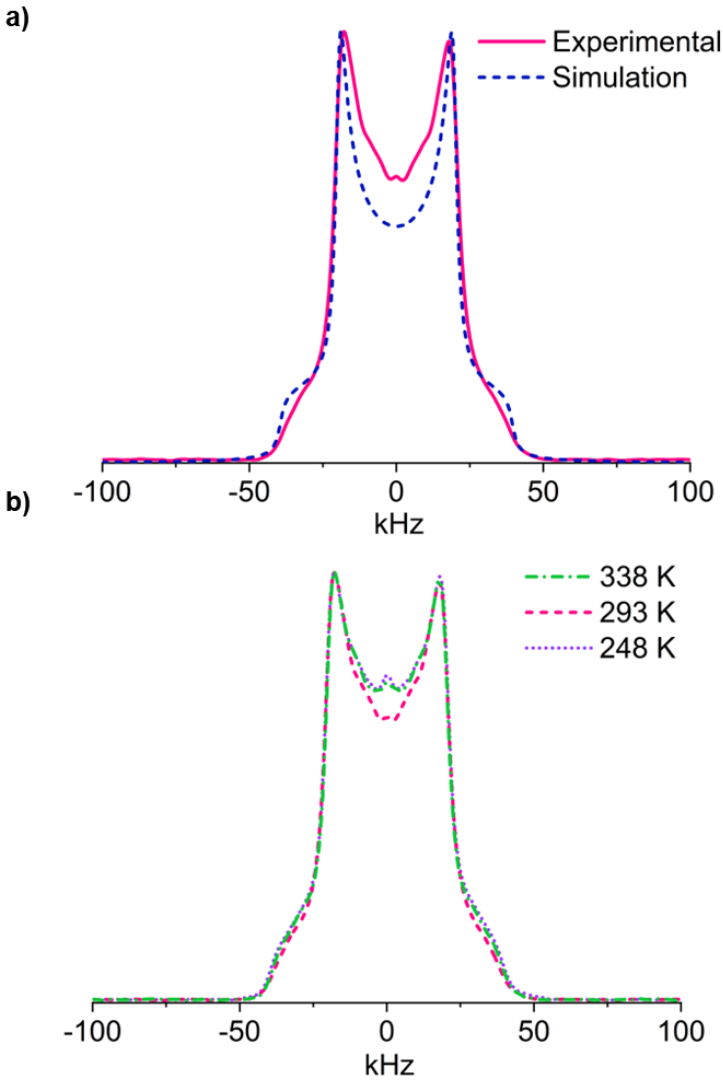


**Figure 7.** $^{2}H$ NMR analyses of the deuterated rotor **I**. a) Comparison between the experimental (solid pink line) and simulated data (dashed blue line) at room temperature, b) Overlay of the spectra of rotor **I** at three temperatures (338 K, 293 K, and 248 K), showing minor changes in the outer shoulders and inner peaks of the deuterium signal.

With the enriched deuterium rotor **I** in our hands, we recorded $^{2}$H NMR spectra using the echo spin technique at different temperatures (**Figure *7*** and **Figure *8***). The experimental spectrum showed two peaks separated by 36.01 kHz at 293 K, confirming that DABCO within the cocrystal undergoes fast motion. We successfully reproduced the experimental data by using a fitting approach through the freely available NMR Weblab interface.[39] The fitted line shape indicates that DABCO experiences a very fast rotation at room temperature (>15 MHz). Moreover, considering the activation barrier to rotation determined through periodic calculations ($E_a$ = 6.8 kcal mol$^{-1}$), we estimated that the rotary portion should experience rotations with 33 MHz frequency, which is in excellent agreement with the fitted data.

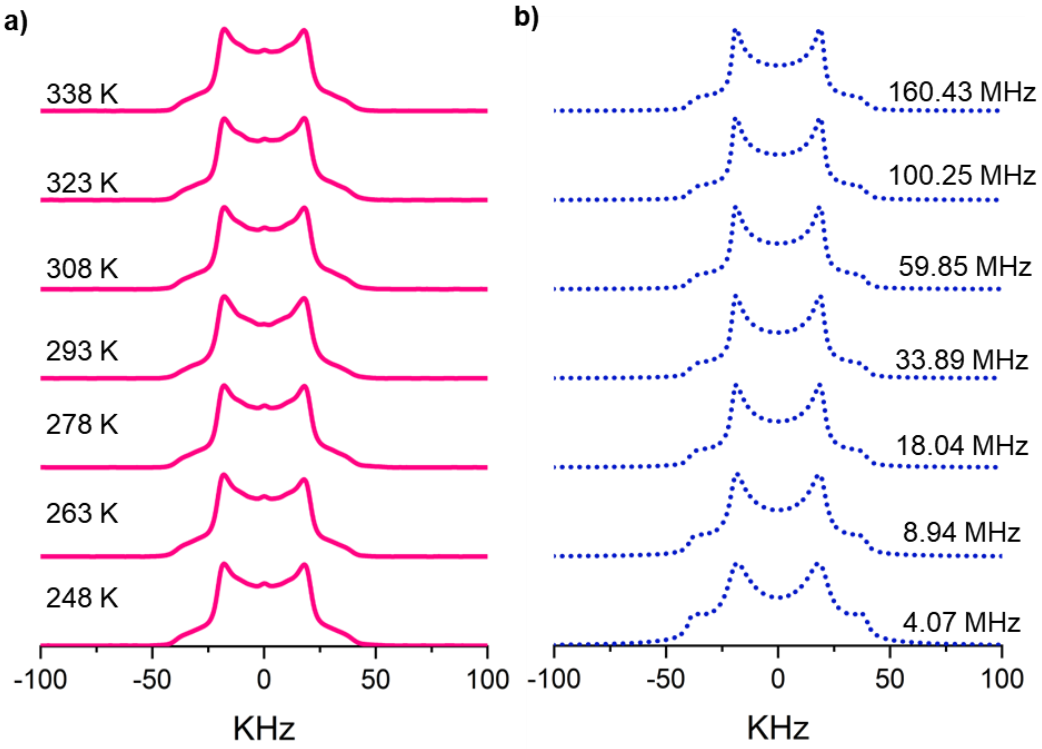


**Figure 8.** Experimental and simulated $^{2}$H NMR spectra of partially deuterated rotor **I** as a function of temperature.

Subsequently, we performed variable temperature $^{2}$H experiments on rotor **I**, ranging from 248 to 338 K, which resulted in only minor changes in the broadness of the spectra. To estimate the rotational frequencies at different temperatures (T), we used the calculated activation energy to rotation and employed a pre-exponential value

$\tau_0^{-1}$ from previously reported rotors ($\tau_0^{-1} = 4x10^{12}\ s^{-1}$),[16] into the Arrhenius equation:

$\tau_c^{-1} = \tau_0^{-1}\, e^{\left(-\frac{E_a}{RT}\right)}$,

where $k_{rot}$ ($\tau_c$) was obtained from K= $\frac{1}{\tau_c}$

By using this approach, we achieved excellent agreement between the fitted line shapes and the experimental data, further supporting the reliability of our DFT computations. The fitting process indicated that with an activation energy of $E_a$ = 6.8 kcal mol$^{-1}$, a rotational frequency of 4.06 MHz is still expected at 248 K.

## Solid-state fluorescence of stators and rotors

*Following the dynamic characterization, our attention turned to the emission properties of the rotors **I** and **III** compared to those of the stators (**ICZ** and **Cy-ICZ**). The emission of indolocarbazoles is regarded as one of their most appealing characteristics, which has been extensively explored in various reported derivatives for diverse applications.[40–42] In this work, we examined the changes in their fluorescence upon cocrystallization. Micrographs of the single crystals of rotors **I** and **III** under white light and UV light are present in*

**Figure *9***. Rotor **I** exhibits blue photoluminescence, whereas rotor **III** shows low emission.

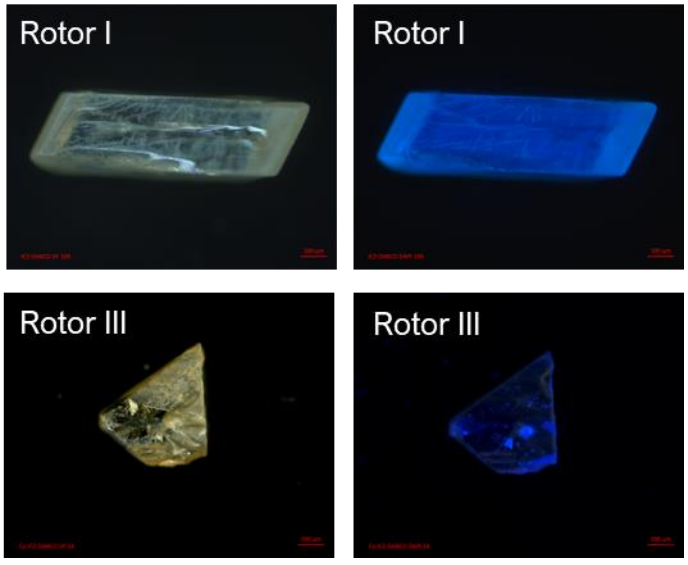

**Figure 9.** Micrographs of rotors **I** and **III** under a) and c) white light, b) and d) under UV excitation.

Table 1. Solid-state photophysical properties in the starting compounds and corresponding Rotors

| | **ICZ** | Rotor **I** | **Cy-ICZ** | Rotor **III** |
|---|---|---|---|---|
| $\lambda_{max}$ exc (nm) | 340 | 340 | 380 | 380 |
| $\lambda_{max}$ em (nm) | 490 | 479 | 448 | 460 |
| QY (%) | 66 | 38 | 9.6 | 2.8 |

While minor variations occurred in the emission maxima (between 10-12 nm), the largest change was observed in the fluorescence quantum yields (QY), with the respective cocrystals exhibiting a substantial decrease in intensity. The final QYs were 35-70 % smaller than the initial values (Table 1 and **Figure 10**). To rationalize the differences in the photophysics, we considered a molecule-centered mechanism similar to the observed in crystalline carbazole and in crystals of carbazole derivatives, which models the different deactivation pathways from the electronically excited crystal in the $S_1$ state.[43–45]

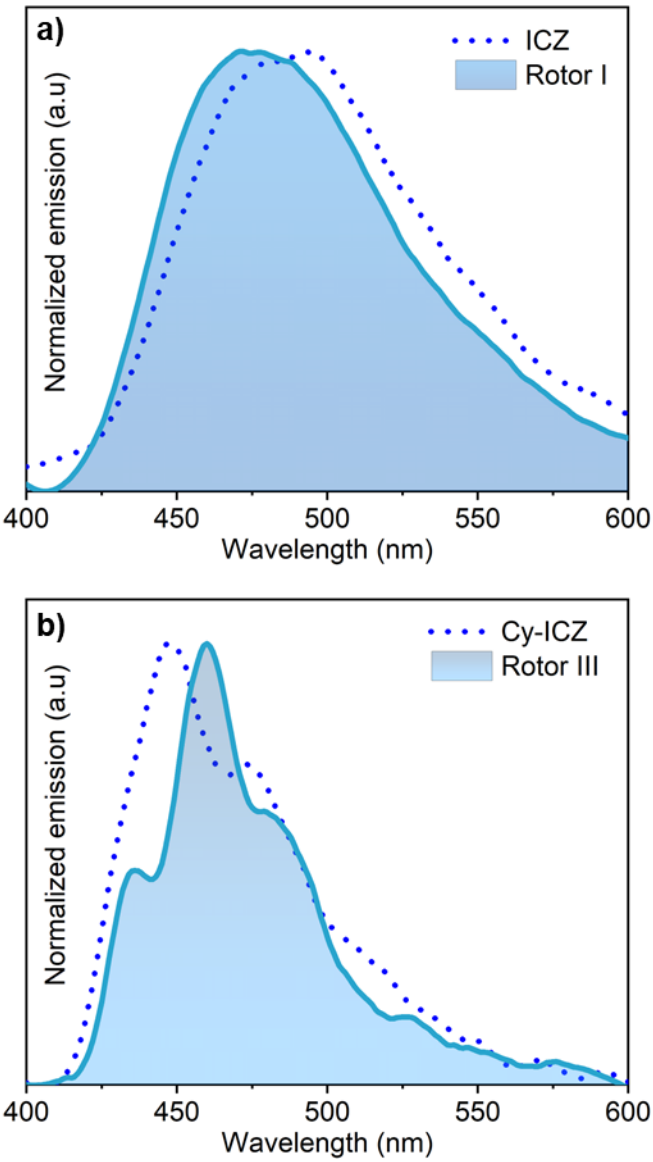


***Figure 10.*** *Solid State fluorescence comparison between a) ICZ and Rotor I and b) Cy-ICz and Rotor III.*

The electronic excitation to $S_1$ occurs via a $\pi$-$\pi^*$ transition localized in the indolocarbazole subunit, computed at 3.23, 3.18, 3.24, and 3.06 eV for **ICz**, rotor **I**, **Cy-ICz**, and rotor **III**, respectively (Table 2 and Figure S21), in good agreement with the experimental absorption maxima (Table 1). Once in the $S_1$ excited state, vibrational cooling drives the system from the Franck-Condon (FC) region to the corresponding minima in $S_1$ ($S_{1min}$). From there, the excited system can radiatively deactivate to the ground state through fluorescence or undergo competing

nonradiative pathways such as internal conversion and intersystem crossing. We modeled the transition rates for these deactivation pathways using the Fermi Golden Rule approach, as described in the Computational Details section (Equations S1-S3).[46] The models used here rely on the harmonic approximation, thus the results should be considered qualitative. The predicted radiative and nonradiative rates are reported in Table 2.

Table 2: Electronic energies (in eV) for the selected transitions, fluorescence $\boldsymbol{k_f}$, internal conversion $\boldsymbol{k_{IC}}$ and intersystem crossing $\boldsymbol{k_{ISC}}$ rate constants (in $s^{-1}$), spin-orbit couplings (SOC, in $cm^{-1}$), and $S_1$-$T_2$ energy gaps computed in the strong coupling limit (in eV) for ICz, rotor I, Cy-ICz, and rotor III in the crystal. All the values obtained at the TD-B3LYP/6-311++G(d,p) level considering point charge embedding (See Computational Details).

| | **ICz** | rotor **I** | **Cy-ICz** | rotor **III** |
|---|---|---|---|---|
| $S_0 \rightarrow S_1$ | 3.23 (π-π*) | 3.18 (π-π*) | 3.24 (π-π*) | 3.06 (π-π*) |
| $S_1 \rightarrow S_0$ | 3.02 (π-π*) | 2.97 (π-π*) | 3.02 (π-π*) | 2.82 (π-π*) |
| $\boldsymbol{k_f}$ | 6.29 x $10^7$ $s^{-1}$ | 4.26 x $10^7$ $s^{-1}$ | 5.42 x $10^7$ $s^{-1}$ | 4.73 x $10^7$ $s^{-1}$ |
| $\boldsymbol{k_{IC}}$ | 1.00 x $10^2$ $s^{-1}$ | 6.00 x $10^2$ $s^{-1}$ | 1.50 x $10^4$ $s^{-1}$ | 8.68 x $10^6$ $s^{-1}$ |
| $\boldsymbol{k_{ISC}}$ | 7.18 x $10^4$ $s^{-1}$ | 1.95 x $10^4$ $s^{-1}$ | 1.81 x $10^6$ $s^{-1}$ | 2.74 x $10^7$ $s^{-1}$ |
| $\boldsymbol{SOC_{S_1T_1}}$ | 0.015 | 0.053 | 0.094 | 0.097 |
| $\boldsymbol{SOC_{S_1T_2}}$ | 0.877 | 0.813 | 0.676 | 0.622 |
| $\Delta\boldsymbol{E_{S_1T_1}}$ | 0.300 | 2.404 | 2.330 | 3.287 |
| $\Delta\boldsymbol{E_{S_1T_2}}$ | 0.228 | 0.268 | 0.130 | 0.054 |

Our main aim here is to elucidate the factors contributing to the different behaviors of ICz and Cy-ICZ and their impact on the quantum yields. The calculated fluorescence rates exhibit similar order of magnitude for the four crystals, indicating that the discrepancy in radiative mechanisms is not likely to determine the QY (Table 2). The internal conversion rate constant ($k_{\mathrm{IC}}$), computed at the FC region within the weak coupling limit,[38] is small for ICZ and rotor **I** (1.00 x $10^2$ $s^{-1}$ and 6.00 x $10^2$ $s^{-1}$ respectively). However, the predicted rates for $k_{\mathrm{IC}}$ increase by a couple of orders of magnitude in Cy-ICz (1.50 x $10^4$ $s^{-1}$) and in rotor **III** (8.68 x $10^6$ $s^{-1}$). A vibronic coupling analysis suggests that the increase in $k_{\mathrm{IC}}$ could be associated with vibrations, particularly where the lateral chain in Cy-ICz has an important role and with intermolecular vibrations between Cy-ICz and the DMF solvent along the hydrogen bond connecting the two molecules. To illustrate the effect of vibrations in Rotor III, we show the vibrations with larger Huang-Rhys factors for the $S_0$-$S_1$ transition in the crystal phase (Figure 11). The plots for the Huang-Rhys factors for Rotor I and a comparison with the gas phase results can be found in the Supplementary Information (Figures S24 and S25).The increase in $k_{\mathrm{IC}}$ for rotor **III** is mainly associated with intermolecular vibrations between the Cy-ICz and the

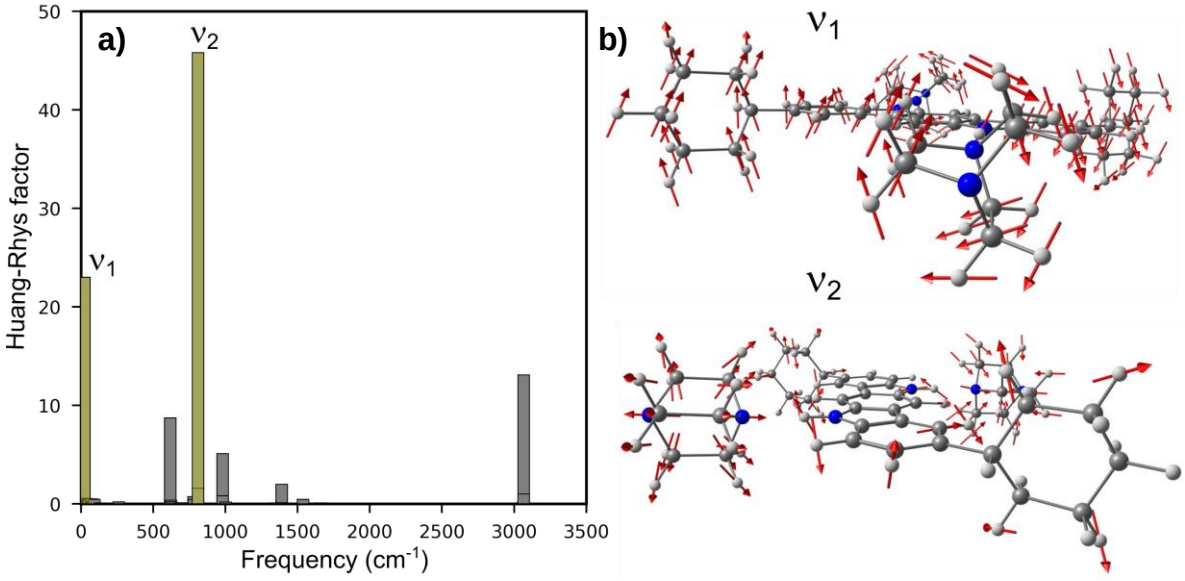


Figure 11: *a) Huang-Rhys factors for the $S_0$-$S_1$ electronic transition of Rotor III. b) The main displacement vectors of the vibrational modes with higher coupling to the electronic transition (highlighted in yellow in a)).*

DABCO moieties, involving restricted intermolecular rotations and vibrations where the side chains also show important reorganization.

Our predicted ISC rates indicate this is an important competing pathway. ISC from $S_1$ to both $T_1$ and $T_2$ is energetically allowed. The ISC rate constants ($k_{\mathrm{ISC}}$) for the $S_1$-$T_2$ transition, predicted for **ICz**, rotor **I**, **Cy-ICz,** and rotor **III**, are 7.18 x $10^4$, 1.95 x $10^4$, 1.81 x $10^6$ and 2.74 x $10^7$ $s^{-1}$, respectively (Table 2). The trend predicted for the studied series suggests that ISC could play a significant role in the deactivation of **Cy-ICz** and rotor **III**. The positive trends predicted for $k_{\mathrm{ISC}}$ align with the negative trend in the fluorescence QYs observed in the experiments (Table I and Table II).

The ISC transition rate is influenced by two main factors, the electronic coupling $\widehat{\mathrm{H}}_{\mathrm{SOC}}$ and the energy gap $\Delta\mathrm{E}$ between the involved states (Equation S3). ISC is facilitated by larger spin-orbit coupling (SOC) values and smaller $\Delta\mathrm{E}$. The first-order SOC values between $S_1$ and $T_1$, as well as between $S_1$ and $T_2$, are relatively small (< 1 $cm^{-1}$, Table 2), consistent with the generalized El Sayed rules.[47] This is expected because all the states ($S_1$, $T_1$, and $T_2$) have a $\pi\pi^*$ character localized on the same subunit, which remains the same across all the studied cases (Figure S21-S23). The energy gap $\Delta\mathrm{E}_{\mathrm{S_1T_1}}$, modeled in the strong coupling limit $\Delta\mathrm{E}_{\mathrm{S_1T_1}} = (\Delta\mathrm{E}^{\mathrm{ad}}_{\mathrm{S_1T1_1}} + \lambda)^2 / 4\lambda$,[36] is large for all the systems (Table 2), making ISC from $S_1$ to $T_1$ improbable. In contrast, the $\Delta\mathrm{E}_{\mathrm{S_1T_2}}$gap is smaller and decreases when going from **ICz**, rotor **I**, **Cy-ICz** to rotor **III**, explaining the increase in the ISC transition rate constant in this series (Table 2). Our computations suggest that the different QYs obtained for these systems are primarily determined by the different nonradiative decay pathways, particularly the potential competition between internal conversion and intersystem crossing, which is facilitated by the additional nonradiative pathways opened by the presence of the rotors.

## Conclusions

Indolo[3,2-*b*]carbazole is a promising candidate for the development of luminescent concatenated rotors, despite its relatively low solubility. It is possible to cocrystallize it by employing an excess of DABCO. The resulting 1D molecular rotors exhibit fast molecular rotation, as revealed by VT SCXRD, DFT periodic computations, and solid state $^{2}$H NMR.

In the case of rotor **I**, the presence of four indolocarbazole molecules surrounding DABCO creates a symmetrical and rigid environment, which explains the high activation energy for rotation of 6.8 kcal mol$^{-1}$. In rotor **III**, the cavity is formed by two rigid molecules and two flexible cyclohexyl fragments, accounting for the asymmetrical potential energy profile and the lower activation energy for rotation of 1.8 kcal mol$^{-1}$. Furthermore, the radiative and nonradiative rate constants indicate that the motion of the DABCO rotators influences the competition of additional nonradiative pathways, thereby reducing the fluorescence quantum yields. ISC appears to be an important nonradiative mechanism for Cy-ICz and rotor **III**. The combination of techniques employed in this work shows that the intramolecular motion in these rotors modifies the photophysical properties of molecular crystals.

**ORCID:**

Ernesto Hernández Morales: 0000-0002-3217-8589

Abraham Colin-Molina: 0000-0002-2425-4254

Jessica Arcudia: 0000-0003-4783-3627

Federico J. Hernández: 0000-0001-7497-9424

Rachel Crespo-Otero: 000-0002-8725-5350

Gabriel Merino: 0000-0003-1961-8321

Braulio Rodríguez-Molina: 0000-0002-1851-9957

## CCDC deposit numbers

2265771-2265780

## Acknowledgments

This work was financially supported by DGAPA PAPIIT IN207222 and CONACYT A1-S-32820. E. H.-M. acknowledges CONACYT for the scholarship (1078913). Computational resources were provided by the CGSTIC (Xiuhcoatl). J. A. thanks CONACYT for supporting her Ph.D. fellowship (859351). We would like to acknowledge the technical assistance of M.Sc. Simón Hernández-Ortega (SCXRD), Dr. M. C. Garcia Gonzalez, Dr. F. J. Pérez Flores (MS), Dr. Martha Elena García Aguilera, M. A. Peña González, M.Sc. Armando Navarro-Huerta, M.Sc Erick Rene Hernández Santiago, M.Sc. E. Huerta Salazar (NMR), Dr. Adriana Romo (IR) and M.Sc. Melina Tapia (PXRD), Dr. Sandra Zetina (Optical Microscopy). Also, technical support from Dr. Diego Martínez Otero (SCXRD) from (CCIQS-UAEMex).R.C-O and F.J. H acknowledge Leverhulme Trust (RPG-2019-122) for funding. We utilized the ARCHER UK National Supercomputing Service (EP/X035859/1) via the Materials Chemistry Consortium and the Molecular Modelling Hub for computational resources, MMM Hub, which is partially funded by EPSRC (EP/T022213/1).

## References

(1) Harada, J.; Ohtani, M.; Takahashi, Y.; Inabe, T. Molecular Motion, Dielectric Response, and Phase Transition of Charge-Transfer Crystals: Acquired Dynamic and Dielectric Properties of Polar Molecules in Crystals. *J. Am. Chem. Soc.* **2015**, *137* (13), 4477–4486. https://doi.org/10.1021/jacs.5b00412.

(2) Setaka, W.; Yamaguchi, K. Thermal Modulation of Birefringence Observed in a Crystalline Molecular Gyrotop. *Proceedings of the National Academy of Sciences* **2012**, *109* (24), 9271–9275. https://doi.org/10.1073/pnas.1114733109.

(3) Jin, M.; Yamamoto, S.; Seki, T.; Ito, H.; Garcia-Garibay, M. A. Anisotropic Thermal Expansion as the Source of Macroscopic and Molecular Scale Motion in Phosphorescent Amphidynamic Crystals. *Angewandte Chemie International Edition* **2019**, *58* (50), 18003–18010. https://doi.org/10.1002/anie.201909048.

(4) Hutchins, K. M.; Unruh, D. K.; Verdu, F. A.; Groeneman, R. H. Molecular Pedal Motion Influences Thermal Expansion Properties within Isostructural Hydrogen-Bonded Co-Crystals. *Crystal Growth & Design* **2018**, *18* (2), 566–570. https://doi.org/10.1021/acs.cgd.7b01386.

(5) So, H.-S.; Minami, T.; Jindo, T.; Matsumoto, S. Thermosalient Effect of Two Polymorphs of a Diketopyrrolopyrrole Dye with Different Crystal Systems and Molecular Arrangements. *CrystEngComm* **2018**, *20* (36), 5317–5320. https://doi.org/10.1039/C8CE00940F.
(6) Sun, L.; Wang, Y.; Yang, F.; Zhang, X.; Hu, W. Cocrystal Engineering: A Collaborative Strategy toward Functional Materials. *Advanced Materials* **2019**, *31* (39), 1902328. https://doi.org/10.1002/adma.201902328.
(7) Ma, S.; Du, S.; Pan, G.; Dai, S.; Xu, B.; Tian, W. Organic Molecular Aggregates: From Aggregation Structure to Emission Property. *Aggregate* **2021**, *2* (4), e96. https://doi.org/10.1002/agt2.96.
(8) Liu, S.; Cheng, Y.; Li, Y.; Chen, M.; Lam, J. W. Y.; Tang, B. Z. Manipulating Solid-State Intramolecular Motion toward Controlled Fluorescence Patterns. *ACS Nano* **2020**, *14* (2), 2090–2098. https://doi.org/10.1021/acsnano.9b08761.
(9) Jin, M.; Ando, R.; Jellen, M. J.; Garcia-Garibay, M. A.; Ito, H. Encapsulating N-Heterocyclic Carbene Binuclear Transition-Metal Complexes as a New Platform for Molecular Rotation in Crystalline Solid-State. *J. Am. Chem. Soc.* **2021**, *143* (2), 1144–1153. https://doi.org/10.1021/jacs.0c11981.
(10) Streckaite, S.; Karpicz, R.; Gruodis, A.; Dehaen, W.; Van Snick, S.; Kirkus, M.; Grigalevicius, S.; Grazulevicius, J. V.; Gulbinas, V. Fluorescence Quenching of Indolo[3,2-b]Carbazole Compounds by Conformational Motions of Attached Substituents. *Dyes and Pigments* **2016**, *133*, 120–126. https://doi.org/10.1016/j.dyepig.2016.05.040.
(11) Nishino, K.; Tanaka, K.; Chujo, Y. Tuning of Sensitivity in Thermochromic Luminescence by Regulating Molecular Rotation Based on Triphenylamine-Substituted o-Carboranes. *Asian Journal of Organic Chemistry* **2019**, *8* (12), 2228–2232. https://doi.org/10.1002/ajoc.201900537.
(12) Jin, M.; Chung, T. S.; Seki, T.; Ito, H.; Garcia-Garibay, M. A. Phosphorescence Control Mediated by Molecular Rotation and Aurophilic Interactions in Amphidynamic Crystals of 1,4-Bis[Tri-(p-Fluorophenyl)Phosphane-Gold(I)-Ethynyl]Benzene. *J. Am. Chem. Soc.* **2017**, *139* (49), 18115–18121. https://doi.org/10.1021/jacs.7b11316.
(13) Tian, Y.; Gong, Y.; Liao, Q.; Wang, Y.; Ren, J.; Fang, M.; Yang, J.; Li, Z. Adjusting Organic Room-Temperature Phosphorescence with Orderly Stimulus-Responsive Molecular Motion in Crystals. *Cell Reports Physical Science* **2020**, *1* (5), 100052. https://doi.org/10.1016/j.xcrp.2020.100052.
(14) Zhao, Z.; Lu, P.; Y. Lam, J. W.; Wang, Z.; K. Chan, C. Y.; Y. Sung, H. H.; D. Williams, I.; Ma, Y.; Zhong Tang, B. Molecular Anchors in the Solid State: Restriction of Intramolecular Rotation Boosts Emission Efficiency of Luminogen Aggregates to Unity. *Chemical Science* **2011**, *2* (4), 672–675. https://doi.org/10.1039/C0SC00521E.
(15) Catalano, L.; Naumov, P. Exploiting Rotational Motion in Molecular Crystals. *CrystEngComm* **2018**, *20* (39), 5872–5883. https://doi.org/10.1039/C8CE00420J.
(16) Colin-Molina, A.; Karothu, D. P.; Jellen, M. J.; Toscano, R. A.; Garcia-Garibay, M. A.; Naumov, P.; Rodríguez-Molina, B. Thermosalient Amphidynamic Molecular Machines: Motion at the Molecular and Macroscopic Scales. *Matter* **2019**, *1* (4), 1033–1046. https://doi.org/10.1016/j.matt.2019.06.018.
(17) Colin-Molina, A.; Jellen, M. J.; Rodríguez-Hernández, J.; Cifuentes-Quintal, M. E.; Barroso, J.; Toscano, R. A.; Merino, G.; Rodríguez-Molina, B. Hydrogen-Bonded

Crystalline Molecular Machines with Ultrafast Rotation and Displacive Phase Transitions. *Chemistry – A European Journal* **2020**, *26* (51), 11727–11733. https://doi.org/10.1002/chem.202001156.
(18) Navarro-Huerta, A.; Jellen, M. J.; Arcudia, J.; Teat, S. J.; Toscano, R. A.; Merino, G.; Rodríguez-Molina, B. Tailoring the Cavities of Hydrogen-Bonded Amphidynamic Crystals Using Weak Contacts: Towards Faster Molecular Machines. *Chem. Sci.* **2021**, *12* (6), 2181–2188. https://doi.org/10.1039/D0SC05899H.
(19) Ji, C.; Li, S.; Deng, F.; Liu, S.; Adnan Asghar, M.; Sun, Z.; Hong, M.; Luo, J. Bistable N–H···N Hydrogen Bonds for Reversibly Modulating the Dynamic Motion in an Organic Co-Crystal. *Physical Chemistry Chemical Physics* **2016**, *18* (16), 10868–10872. https://doi.org/10.1039/C6CP01073C.
(20) Marivel, S.; Braga, D.; Grepioni, F.; Lampronti, G. I. Mechanochemical Preparation of Adducts (Co-Crystals and Molecular Salts) of 1,4-Diazabicyclo-[2.2.2]-Octane with Aromatic Polycarboxylic Acids. *CrystEngComm* **2010**, *12* (7), 2107–2112. https://doi.org/10.1039/B922915A.
(21) Dabros, M.; Emery, P. R.; Thalladi, V. R. A Supramolecular Approach to Organic Alloys: Cocrystals and Three- and Four-Component Solid Solutions of 1,4-Diazabicyclo[2.2.2]Octane and 4-X-Phenols (X=Cl, CH3, Br). *Angewandte Chemie International Edition* **2007**, *46* (22), 4132–4135. https://doi.org/10.1002/anie.200604830.
(22) Ye, H.-Y.; Ge, J.-Z.; Chen, F.; Xiong, R.-G. Reversible Phase Transition of the 1:1 Co-Crystal of 1,4-Diazabicyclo-[2.2.2]Octane ( DABCO ) and Hydroquinone ,. *CrystEngComm* **2010**, *12* (6), 1705–1708. https://doi.org/10.1039/B923314H.
(23) Jiang, X.; Duan, H.-B.; Jellen, M. J.; Chen, Y.; Chung, T. S.; Liang, Y.; Garcia-Garibay, M. A. Thermally Activated Transient Dipoles and Rotational Dynamics of Hydrogen-Bonded and Charge-Transferred Diazabicyclo [2.2.2]Octane Molecular Rotors. *J. Am. Chem. Soc.* **2019**, *141* (42), 16802–16809. https://doi.org/10.1021/jacs.9b07518.
(24) Janosik, T.; Rannug, A.; Rannug, U.; Wahlström, N.; Slätt, J.; Bergman, J. Chemistry and Properties of Indolocarbazoles. *Chem. Rev.* **2018**, *118* (18), 9058–9128. https://doi.org/10.1021/acs.chemrev.8b00186.
(25) Stojaković, J.; Whitis, A. M.; MacGillivray, L. R. Discrete Double-to-Quadruple Aromatic Stacks: Stepwise Integration of Face-to-Face Geometries in Cocrystals Based on Indolocarbazole. *Angewandte Chemie International Edition* **2013**, *52* (46), 12127–12130. https://doi.org/10.1002/anie.201304615.
(26) Liu, C.-H.; Niazi, M. R.; Perepichka, D. F. Strong Enhancement of π-Electron Donor/Acceptor Ability by Complementary DD/AA Hydrogen Bonding. *Angewandte Chemie International Edition* **2019**, *58* (48), 17312–17321. https://doi.org/10.1002/anie.201910288.
(27) Guo, J.; Zeng, Y.; Zhen, Y.; Geng, H.; Wang, Z.; Yi, Y.; Dong, H.; Hu, W. Non-Equal Ratio Cocrystal Engineering to Improve Charge Transport Characteristics of Organic Semiconductors: A Case Study on Indolo[2,3-a]Carbazole. *Angewandte Chemie* **2022**, *134* (28), e202202336. https://doi.org/10.1002/ange.202202336.
(28) Bintinger, J.; Yang, S.; Fruhmann, P.; Holzer, B.; Stöger, B.; Svirkova, A.; Marchetti-Deschmann, M.; Horkel, E.; Hametner, C.; Fröhlich, J.; Kymissis, I.; Mikula, H. Synthesis, Characterization and Printing Application of Alkylated Indolo[3,2-

b]Carbazoles. *Synthetic Metals* **2017**, *228*, 9–17. https://doi.org/10.1016/j.synthmet.2017.04.003.
(29) Zhao, H.; Jiang, L.; Dong, H.; Li, H.; Hu, W.; Ong, B. S. Influence of Intermolecular N□H···π Interactions on Molecular Packing and Field-Effect Performance of Organic Semiconductors. *ChemPhysChem* **2009**, *10* (13), 2345–2348. https://doi.org/10.1002/cphc.200900249.
(30) Biscaia, I. F. B.; Gomes, S. N.; Bernardi, L. S.; Oliveira, P. R. Obtaining Cocrystals by Reaction Crystallization Method: Pharmaceutical Applications. *Pharmaceutics* **2021**, *13* (6), 898. https://doi.org/10.3390/pharmaceutics13060898.
(31) Chaudhary, A.; Mohammad, A.; Mobin, S. M. Recent Advances in Single-Crystal-to-Single-Crystal Transformation at the Discrete Molecular Level. *Crystal Growth & Design* **2017**, *17* (5), 2893–2910. https://doi.org/10.1021/acs.cgd.7b00154.
(32) Shi, P.-P.; Tang, Y.-Y.; Li, P.-F.; Liao, W.-Q.; Wang, Z.-X.; Ye, Q.; Xiong, R.-G. Symmetry Breaking in Molecular Ferroelectrics. *Chem. Soc. Rev.* **2016**, *45* (14), 3811–3827. https://doi.org/10.1039/C5CS00308C.
(33) Ning, W.-H.; Zhai, L.; Ren, X.-M. Two-Step Dielectric Anomalies Coupled with Structural Phase Transitions in a Co-Crystal of 1,4-Diazabicyclo[2.2.2]Octane and 4,4′-Biphenol. *RSC Advances* **2014**, *4* (59), 30993–30998. https://doi.org/10.1039/C4RA03681F.
(34) Mills, G.; Jónsson, H.; Schenter, G. K. Reversible Work Transition State Theory: Application to Dissociative Adsorption of Hydrogen. *Surface Science* **1995**, *324* (2), 305–337. https://doi.org/10.1016/0039-6028(94)00731-4.
(35) Johnson, E. R.; Keinan, S.; Mori-Sánchez, P.; Contreras-García, J.; Cohen, A. J.; Yang, W. Revealing Noncovalent Interactions. *J. Am. Chem. Soc.* **2010**, *132* (18), 6498–6506. https://doi.org/10.1021/ja100936w.
(36) Contreras-García, J.; Johnson, E. R.; Keinan, S.; Chaudret, R.; Piquemal, J.-P.; Beratan, D. N.; Yang, W. NCIPLOT: A Program for Plotting Noncovalent Interaction Regions. *J. Chem. Theory Comput.* **2011**, *7* (3), 625–632. https://doi.org/10.1021/ct100641a.
(37) Hansen, M. R.; Graf, R.; Spiess, H. W. Solid-State NMR in Macromolecular Systems: Insights on How Molecular Entities Move. *Acc. Chem. Res.* **2013**, *46* (9), 1996–2007. https://doi.org/10.1021/ar300338b.
(38) Catalano, L.; Pérez-Estrada, S.; Terraneo, G.; Pilati, T.; Resnati, G.; Metrangolo, P.; Garcia-Garibay, M. A. Dynamic Characterization of Crystalline Supramolecular Rotors Assembled through Halogen Bonding. *J. Am. Chem. Soc.* **2015**, *137* (49), 15386–15389. https://doi.org/10.1021/jacs.5b10776.
(39) Macho, V.; Brombacher, L.; Spiess, H. W. The NMR-WEBLAB: An Internet Approach to NMR Lineshape Analysis. *Appl. Magn. Reson.* **2001**, *20* (3), 405–432. https://doi.org/10.1007/BF03162288.
(40) Zhao, H.-P.; Wang, F.-Z.; Yuan, C.-X.; Tao, X.-T.; Sun, J.-L.; Zou, D.-C.; Jiang, M.-H. Indolo[3,2-b]Carbazole: Promising Building Block for Highly Efficient Electroluminescent Materials. *Organic Electronics* **2009**, *10* (5), 925–931. https://doi.org/10.1016/j.orgel.2009.04.019.
(41) Belletête, M.; Blouin, N.; Boudreault, P.-L. T.; Leclerc, M.; Durocher, G. Optical and Photophysical Properties of Indolocarbazole Derivatives. *J. Phys. Chem. A* **2006**, *110* (51), 13696–13704. https://doi.org/10.1021/jp066143a.

(42) Jia, W.; Wang, H.; Yang, L.; Lu, H.; Kong, L.; Tian, Y.; Tao, X.; Yang, J. Synthesis of Two Novel Indolo[3,2- b ]Carbazole Derivatives with Aggregation-Enhanced Emission Property. *Journal of Materials Chemistry C* **2013**, *1* (42), 7092–7101. https://doi.org/10.1039/C3TC31590H.
(43) J. Hernández, F.; Crespo-Otero, R. Excited State Mechanisms in Crystalline Carbazole: The Role of Aggregation and Isomeric Defects. *Journal of Materials Chemistry C* **2021**, *9* (35), 11882–11892. https://doi.org/10.1039/D1TC02019F.
(44) Sidat, A.; J. Hernández, F.; Stojanović, L.; J. Misquitta, A.; Crespo-Otero, R. Competition between Ultralong Organic Phosphorescence and Thermally Activated Delayed Fluorescence in Dichloro Derivatives of 9-Benzoylcarbazole. *Physical Chemistry Chemical Physics* **2022**, *24* (48), 29437–29450. https://doi.org/10.1039/D2CP04802G.
(45) Rodríguez-Cortés, L. A.; Hernández, F. J.; Rodríguez, M.; Toscano, R. A.; Jiménez-Sánchez, A.; Crespo-Otero, R.; Rodríguez-Molina, B. Conformational Emissive States in Dual-State Emitters with Benzotriazole Acceptors. *Matter* **2023**, *6* (4), 1140–1159. https://doi.org/10.1016/j.matt.2023.01.015.
(46) Hernández, F. J.; Crespo-Otero, R. Modeling Excited States of Molecular Organic Aggregates for Optoelectronics. *Annual Review of Physical Chemistry* **2023**, *74* (1), 547–571. https://doi.org/10.1146/annurev-physchem-102822-100945.
(47) Marian, C. M. Understanding and Controlling Intersystem Crossing in Molecules. *Annual Review of Physical Chemistry* **2021**, *72* (1), 617–640. https://doi.org/10.1146/annurev-physchem-061020-053433.